APPLIED SCIENCES AND ENGINEERING

Human and mouse bones physiologically integrate in a humanized mouse model while maintaining species-specific ultrastructure

I. Moreno-Jiménez[1,2], A. Cipitria[1], A. Sánchez-Herrero[2], A. F. van Tol[1], A. Roschger[1], C. A. Lahr[2], J. A. McGovern[2], D. W. Hutmacher[1,2*†], P. Fratzl[1*†]

Humanized mouse models are increasingly studied to recapitulate human-like bone physiology. While human and mouse bone architectures differ in multiple scales, the extent to which chimeric human-mouse bone physiologically interacts and structurally integrates remains unknown. Here, we identify that humanized bone is formed by a mosaic of human and mouse collagen, structurally integrated within the same bone organ, as shown by immunohistochemistry. Combining this with materials science techniques, we investigate the extracellular matrix of specific human and mouse collagen regions. We show that human-like osteocyte lacunar-canalicular network is retained within human collagen regions and is distinct to that of mouse tissue. This multiscale analysis shows that human and mouse tissues physiologically integrate into a single, functional bone tissue while maintaining their species-specific ultrastructural differences. These results offer an original method to validate and advance tissue-engineered human-like bone in chimeric animal models, which grow to be eloquent tools in biomedical research.

INTRODUCTION

Regardless of the extensive volume of basic biology knowledge acquired from rodent studies, there are major drawbacks to mouse models when translating into human biology. More than a few foundations of the mouse anatomy and physiology show distinct differences with those of humans (*1*). In this context, humanized mice have begun to fill this research gap, thus becoming important preclinical tools for biomedical research. The increasing capacity to genetically engineer a humanized genome in mouse models has allowed studying a variety of conditions such as autoimmunity, infections, graft-versus-host disease, and cancer. Hence, humanized mice aim to become the benchmark research models for biomedicine (*2*–*4*). In particular for primary and secondary bone cancer research, humanized mice have been studied to recreate a human-like bone microenvironment, namely, humanized bone, which can interact with human cancer cells and, hence, recapitulate the cascade of events in tumor progression (*5*–*8*). In this way, we and others have tissue-engineered humanized bone reproducibly with different human cell donors to study bone metastases and primary bone cancers (*5*–*8*). For detailed information about the technical aspects of tissue-engineered humanized bone and its characterization and applications, see (*5*, *9*–*14*). Briefly, humanized bone is tissue-engineered following the implantation of human bone progenitor cells, in combination with a scaffold and growth factors [bone morphogenetic protein (BMP)]. This tissue-engineered construct then forms an ossicle that recapitulates features of the organ bone such as mineralized bone tissue, bone marrow, and a hematopoietic compartment (*15*–*17*). Despite the implantation of bone-forming cells, the co-delivery of BMP is critical for the formation of the tissue-engineered bone organ, as the amount of ectopic bone formed is proportional to the BMP dose (*9*, *18*–*20*). Human cells and extracellular matrix (ECM) interface with host mouse bone tissue, thus making this tissue a human/mouse bone chimera (*9*, *15*, *21*). To further humanize the bone ossicle, mice have also been injected with human hematopoietic stem cells, which have shown to be home not only to the bone marrow of the ossicle but also to the mouse skeleton (*9*, *16*). More recent studies have tissue-engineered bone around the mouse femur, thus creating an ectopic bone ossicle in a clinically more relevant skeletal (i.e., orthotopic) location (*14*).

Often neglected by the research community, the ultrastructural composition of the humanized ossicle is just as important as the molecular and cell biological aspects of these new preclinical models. Since human and mouse bones essentially differ in their tissue architecture (*22*–*24*), the hybrid nature of the humanized bone organ is a fundamental, yet widely understudied, feature. It is well known that alterations in bone composition and structure play a critical role in diseases that use the organ bone as a niche (e.g., osteoporosis and osteogenesis imperfecta) and have an effect on the onset of breast cancer bone metastasis (*25*). Bone is a hierarchically organized organ that serves as a calcium reservoir, hematopoietic compartment, and structural support to the body. At the tissue level, bone is formed by a dense, cortical shell that provides mechanical support and encloses the bone marrow and trabecular (spongy) bone. While in humans and large animals (e.g., pigs, goats, and old sheep) the cortical bone is organized in osteon units formed by concentric layers of collagen (lamellae) around a central vessel canal (fig. S1, E and F), these structures do not exist in mice (fig. S1, C and D) (*22*). Moreover, mice do not have alternating orientations of collagen fibers, namely, plywood structure, that provide strength to lamellar bone (*23*). At the cellular level, both cortical and trabecular bones contain bone cells buried in the mineralized matrix (osteocytes) that live in microcavities (lacunae) and are interconnected via nanometer-scale channels, named canaliculi (*24*). This osteocyte lacunar-canalicular network (LCN) allows cell-to-cell communication and transmits local mechanical stimuli, which, in turn, directs bone formation by osteoblasts, resorption by osteoclasts, and, in large,

[1]Max Planck Institute of Colloids and Interfaces, Department of Biomaterials, Potsdam, Germany. [2]Institute of Health Biomedical Innovation (IHBI), Queensland University of Technology, Brisbane, Australia.
*These authors contributed equally to this work.
†Corresponding author. Email: dietmar.hutmacher@qut.edu.au (D.W.H.); peter.fratzl@mpikg.mpg.de (P.F.)

bone homeostasis (*26*). Recent investigations showed that cellular and tissue levels in bone are structurally coordinated, as the orientation and architecture of the LCN mirror that of the surrounding ECM (*22*). We have previously shown that in an organized ECM (e.g., lamellar bone), the LCN is denser and follows a similar orientation as the collagen fibers, whereas in a disorganized ECM (e.g., woven bone), the LCN shows a more chaotic arrangement and sparser canaliculi (*27*–*31*). Considering that the LCN has also been shown to display differences between human and mouse bone in terms of canalicular density (*28*, *31*, *32*), this might be a distinct morphological feature to examine the ultrastructure of humanized bone.

Although the presence of human ECM and human cells in the humanized bone ossicle has been confirmed using immunohistochemistry (IHC) (*5*, *9*, *17*, *33*), the vasculature remains host (mouse) derived, and thus, it cannot be excluded that mouse progenitor cells additionally contribute to tissue formation in the humanized bone. Moreover, it is known that human cancer cells not only migrate to the humanized bone but also spread into other mouse organs, including the skeleton (*7*, *17*, *34*, *35*). In this context, the question of how much of this humanized bone is actually "human" becomes particularly important, as the interaction of human cancer cells with only the mouse component of this chimeric tissue would defeat the purpose of the model. Furthermore, it remains unknown whether the newly synthesized ECM reflects human or mouse tissue architecture. Here, we hypothesize that the human component of the tissue-engineered bone retains a human-like bone ultrastructure and is distinct from mouse bone formed under the same conditions. To test this hypothesis, we used advanced materials science techniques in combination with IHC to dissect species-specific differences at the bone ultrastructural level. For this aim, we have generated humanized bone based on previously established protocols used to conduct cancer research (*6*, *9*, *12*, *14*). Here, we show that the humanized bone ossicle is a human/mouse chimera. Mouse and human tissue types coexist and structurally integrate within the bone ossicle while maintaining species-specific ultrastructural differences.

RESULTS

Structural integration of the humanized ossicle with native mouse bone

We first examined how the humanized ossicle, formed at an orthotopic location (i.e., skeletal), integrated with the native, host (mouse) bone tissue. To address this, scaffolds seeded with primary human osteoblasts (hOBs) or no osteoblasts were laid down on the lateral site of the mouse femur diaphysis (Fig. 1A and fig. S2C). Bone formation was monitored in vivo using micro–computed tomography (microCT) for 6 weeks and showed a peak 2 weeks after implantation, which significantly reduced by weeks 4 and 6 (fig. S3, A to C). No differences in bone volume were found between human cell–seeded scaffolds and controls (fig. S3, B and C). The humanized ossicle contained trabecular bone and marrow confined by a highly mineralized shell-like tissue and was located in the lateral part of the mouse femur diaphysis [see dashed lines in Fig. 1 (B to D)]. Lateral and medial native femoral cortices showed a different morphology, depending on their physical contact with the newly formed ossicle (Fig. 1C, dashed line). Notably, the lateral femoral cortex, in direct contact with the ossicle, appeared discontinued and remodeled into trabecular bone, compared to the cortical architecture of the medial cortex (Fig. 1, C and D, and movie S1). The trabecular bone formed within the ossicle shell was connected to the highly remodeled lateral cortex, indicative of the strong interaction between the humanized and native (mouse) host tissue (Fig. 1, C and D). Thus, these results indicate that implantation of hOBs-seeded scaffolds results in the formation of an ossicle that physically integrates with the native (mouse) bone tissue.

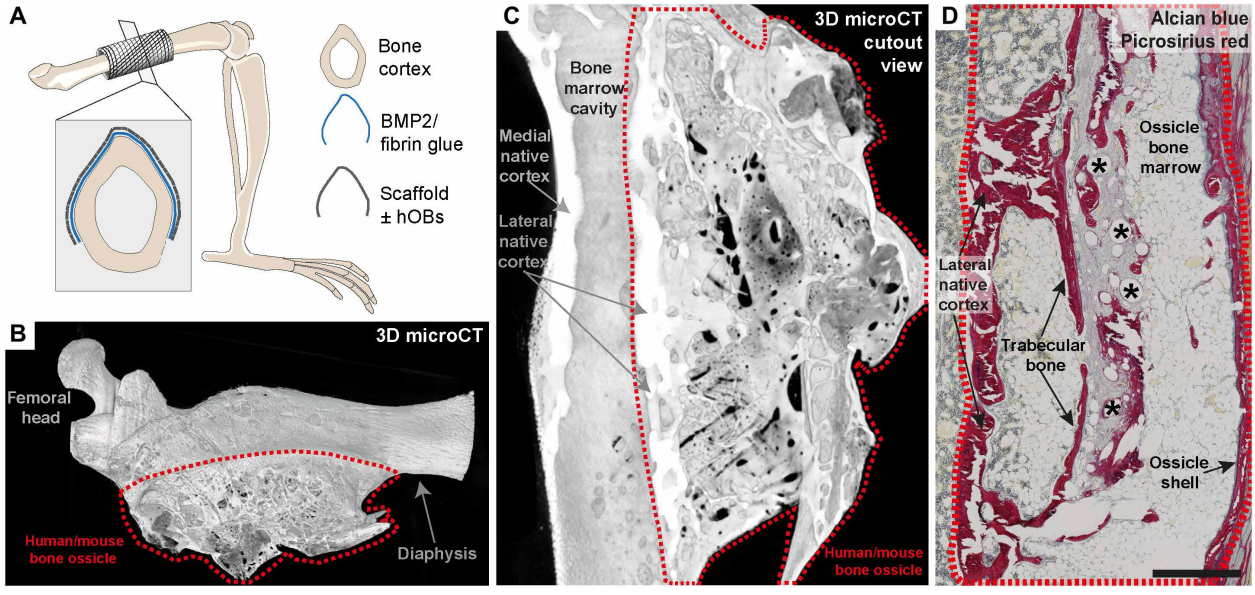

Fig. 1. Humanized bone ossicle forms around the mouse femur after implantation of hOBs-seeded scaffolds. (**A**) Precultured scaffolds with primary hOBs or no cells (scaffold only) were implanted around the lateral part of the bone femur together with BMP2 and fibrin glue. (**B** and **C**) microCT scan rendering of harvested scaffolds 6 weeks after implantation. (**D**) Longitudinal histological section stained with Alcian blue (proteoglycans) and Picrosirius red (collagen). Asterisks indicate scaffold fibers; the dashed line indicates human/mouse bone ossicle. Scale bar, 500 μm. 3D, three-dimensional.

Human and mouse collagen interconnect in vivo in a bone chimera

To investigate the nature of the human-mouse bone interaction, we used IHC to detect regions of human-specific collagen type I (hCol) and distinguish it from mouse collagen type I in hOBs scaffolds. IHC was conducted in consecutive sections together with Picrosirius red staining, which showed in pink the formation of a bone ossicle shell (see dashed line) containing the trabecular bone tissue (Fig. 2A). Neither the femoral cortices nor the ossicle shell showed hCol staining, indicating the mouse origin of the tissue (see dashed line in Fig. 2B). We found, however, that trabecular bone enclosed within the ossicle shell formed an aggregate of both positive and negative hCol-stained regions [see trabecular bone within dashed lines in Fig. 2 (A and B)]. While some trabeculae showed no hCol staining at all (Fig. 2C), others showed strong expression of hCol (Fig. 2E). This finding was further validated by staining consecutive sections with hCol and mouse-specific collagen type I (mCol) staining, which again showed the hybrid hCol/mCol nature of the trabeculae in the ossicle (fig. S4, F and G). We also detected human-specific osteocalcin (hOCalcin), which showed positive staining in regions of trabecular bone within the ossicle (fig. S7, A and B). To determine whether hCol staining correlated with the presence of human osteocytes, consecutive sections were stained with human nuclear mitotic apparatus (hNuma; Fig. 2, D and F). Positive hNuma staining was detected in $hCol^+$ trabeculae (irregular dashed line), indicative of human osteocytes. Interestingly, hNuma staining was also present around scaffold fibers (see asterisks) and around $hCol^+$ trabecular bone (see positive hNuma cells around the irregular dashed line in Fig. 2F). This hNuma staining colocalized with $hCol^+$ staining of the ECM fibers in the bone marrow stroma, indicating the presence of active hOBs producing human collagen matrix. No hNuma staining was apparent in areas of negative hCol staining (Fig. 2, C and D). In summary, these data show that the humanized ossicle is formed by a chimera of human and mouse cells and ECM, which, together, take shape in the form of a chimeric bone organ.

Human collagen regions are structurally different from those of mouse collagen formed under the same conditions

Next, we wanted to address whether human and mouse regions, closely integrated in the ossicle, differed at the ultrastructural level. To do so, trabeculae from hOBs scaffolds were compared with trabeculae from scaffold-only bone ossicles (fig. S5, A and B). To rule out that the presence of cells in the scaffold (and not specifically human ones) influenced the ECM architecture, we included mCherry-labeled mouse osteoblasts (mOBs)–seeded scaffolds as control (fig. S5, C and D). IHC was used to detect the regions of interest (ROIs), which were correlatively imaged with rhodamine staining to visualize the

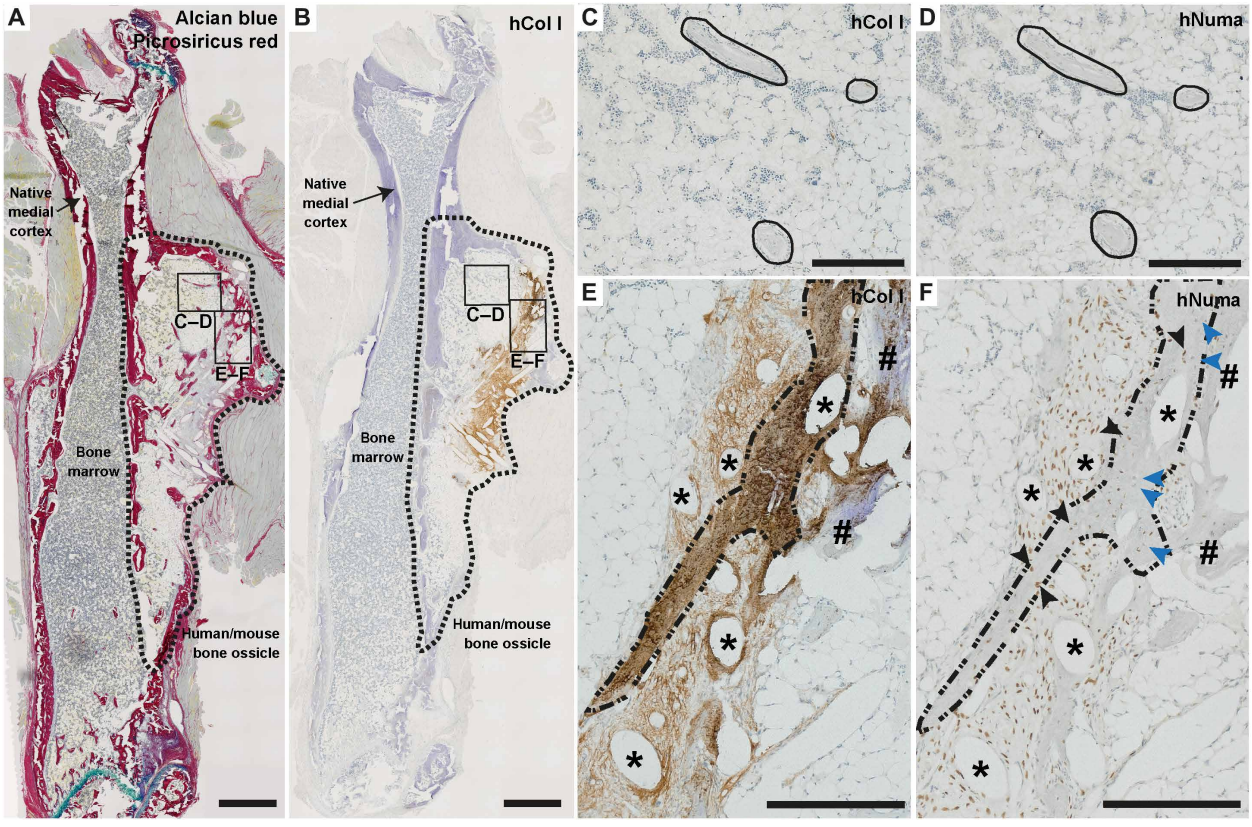

Fig. 2. Human bone integrates and coexists with mouse bone after 6 weeks in vivo. Consecutive longitudinal sections from hOBs-seeded scaffolds stained with Consecutive longitudinal sections from hOBs-seeded scaffolds. (**A**) Stained with Alcian blue (proteoglycans) and Picrosirius red (collagen). (**B**, **C**, and **E**) stained for hCol. (**D**) and (**F**) stained with hNuma. Regular dashed lines (A and B) show the contour of the human/mouse orthotopic bone ossicle. Detailed areas of (C and D) negative (solid line) and (E and F) positive hCol expression (irregular dashed line) were stained with (D and F) hNuma to identify human cells. Brown indicates positive immunostaining for hCol and hNuma; blue indicates nuclei (hematoxylin) counterstain. Asterisks indicate scaffold fibers. Hash indicates bone tissue not stained with hCol. Black and blue arrowheads point to positive and negative hNuma cells, respectively. Scale bars, (A and B) 1000 μm and (C to F) 250 μm.

LCN and with second harmonic generation (SHG) imaging collagen organization (Fig. 3, A to F). The morphology of the LCN in hCol$^+$ regions showed a sparser canalicular network and bulkier lacunae, compared to the LCN in mCherry$^+$ regions (Fig. 3, B and E). Moreover, lacunae in hCol$^+$ trabeculae exhibited heterogeneous morphologies, compared to the elongated, fusiform shape of lacunae in mCherry$^+$ trabeculae (Fig. 3, B and E). LCN analysis showed that canalicular density was significantly lower in hCol$^+$ trabeculae (0.07 ± 0.015 μm/μm^3), compared to scaffold-only and mCherry$^+$ trabeculae [0.012 ± 0.01 and 0.014 ± 0.02 μm/μm^3, respectively; P = 0.001, analysis of variance (ANOVA) with Tukey's post hoc test]. Consistently with a lower canalicular density, average lacuna volume was significantly higher in hCol$^+$ regions compared to mCherry$^+$ lacunae (555.67 ± 57 versus 374.65 ± 165 μm^3; P = 0.038, ANOVA with Tukey's post hoc test). For a qualitative comparison of the human and mouse LCN and collagen arrangement in native bone, see fig. S1. No differences were observed in canalicular density or lacunae size between mCherry$^+$ and scaffold-only trabeculae, and this was expected because of their shared mouse origin.

Corresponding SHG images revealed that hCol$^+$ trabeculae showed a highly interwoven mesh of collagen, compared to mCherry$^+$ areas, where collagen fibers were arranged in a radial orientation parallel to each other (Fig. 3, C and F). The higher ECM organization in mCherry$^+$ trabeculae was consistent with the LCN appearance, where lacunae were oriented following the collagen fiber direction and canaliculi arranged perpendicularly (Fig. 3, B and C). To semiquantify the distinct patterns of collagen organization, we scored the images as lamellar-like (Fig. 3C), intermediate, or woven-like (Fig. 3F). hCol$^+$ regions showed a woven-like collagen organization in 74% of the evaluated volumes, compared to a 26% in mCherry$^+$ and 0% scaffold-only trabeculae, indicating a predominant disorganized ECM in regions of human collagen. Hence, these

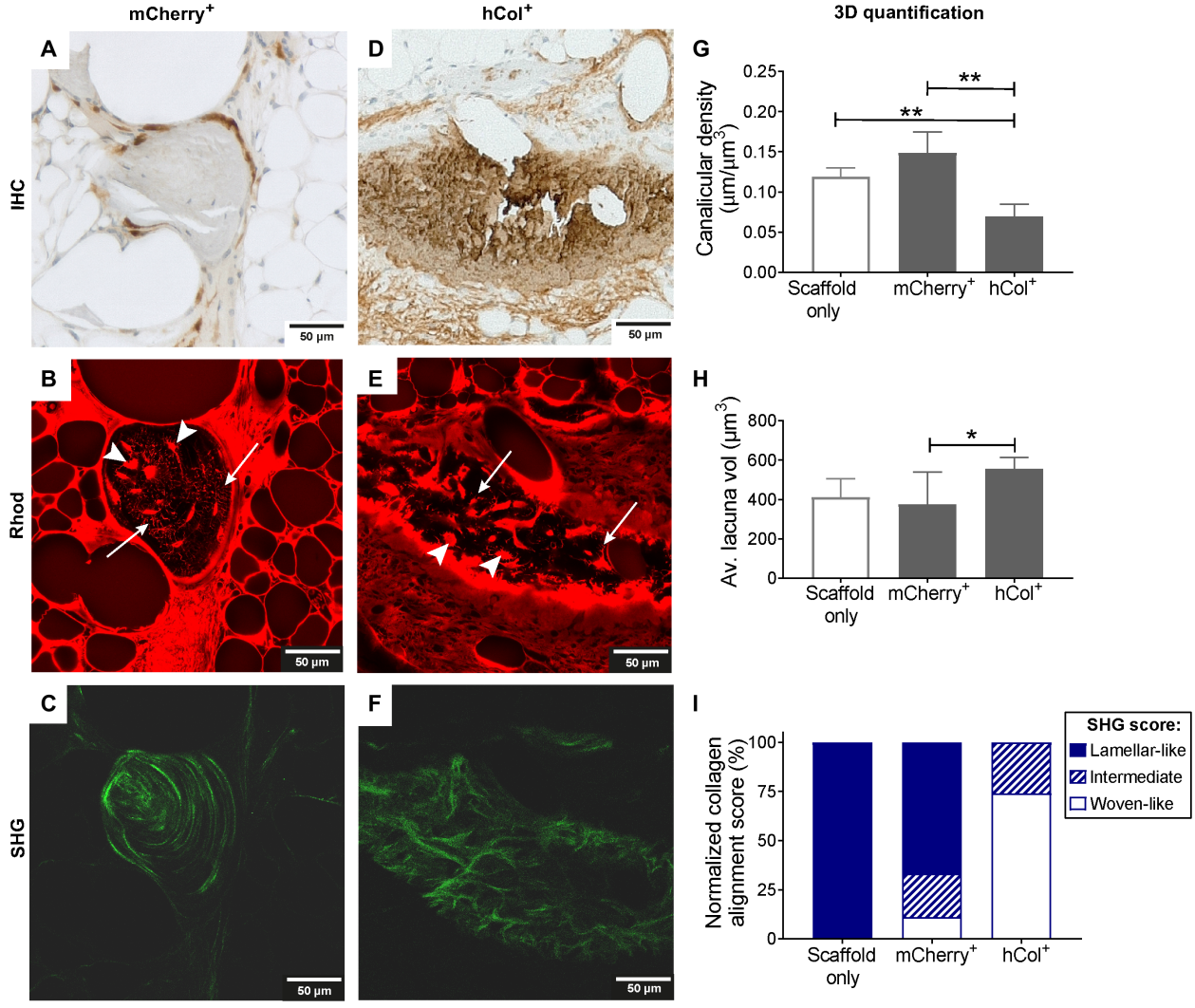

Fig. 3. Osteocyte LCN and collagen architecture are different in human bone (hCol$^+$) compared to mouse bone formed under the same conditions. ROIs of (**A** to **C**) mCherry$^+$ mouse osteoblasts or (**D** to **F**) hCol$^+$ human collagen tissue, detected with (A and D) IHC, (B and E) rhodamine (Rhod) staining of LCN, and (C and F) SHG imaging of collagen. Arrowheads indicate osteocyte lacunae, and arrows indicate canaliculi. Measurements of (**G**) canalicular density (total length of the canaliculi per unit volume), (**H**) average lacuna volume, and (**I**) normalized collagen alignment score classifying into (C) lamellar-like, intermediate, and (F) woven-like bone structure were quantified in the ROIs of each group and normalized with respect to analyzed volume. (G and H) Data represent means ± SD, one-way ANOVA, *P < 0.05 and **P < 0.001. (G and I) n = 2 to 3 ROIs per animal, and N = 6 animals per group.

results indicate that even if hCol$^+$ regions strongly interact with mouse bone, their LCN and ECM architecture is distinct to that of mouse collagen formed under the same conditions.

Chimeric bone exhibits species-specific differences within the same trabecular tissue

After discerning significant differences between human (hCol$^+$) and mouse (mCherry$^+$) in terms of collagen organization and LCN, next, we asked whether similar differences could be observed between trabeculae formed by implanted (human; hCol$^+$) and host (mouse; hCol$^-$) osteoblasts. The LCNs of hCol$^-$ and hCol$^+$ trabeculae were analyzed within the hOBs scaffold group [see Fig. 2 (C and E)] and again showed a significantly lower canalicular density in hCol$^+$ trabeculae ($0.07 \pm 0.15\ \mu m/\mu m^3$) compared to hCol$^-$ ($0.13 \pm 0.28\ \mu m/\mu m^3$; $P = 0.0004$, paired t test; Fig. 4D). In contrast to this, no significant differences in LCN were found between mouse-implanted osteoblasts (mCherry$^+$) and host-derived (mCherry$^-$) trabeculae (Fig. 4E), indicating that the difference in canalicular densities between hCol$^-$ and hCol$^+$ was due to a species-specific effect and not due to the sole presence of precultured osteoblasts in the scaffold. In accordance with this, analysis of trabeculae of mouse origin (scaffold only, mCherry$^+$, mCherry$^-$, and hCol$^-$) displayed comparable canalicular densities (Fig. 4, D to F).

We then aimed to compare the measurements of the ossicle's trabeculae with those of native mouse bone as control. To do so, we included regions of native mouse cortex not in contact with the scaffold [see as reference the medial proximal femoral cortex in Fig. 2 (A and B)and fig. S6] as internal controls in each experimental group (hOBs, $0.21 \pm 0.02\ \mu m/\mu m^3$; mOBs, $0.22 \pm 0.02\ \mu m/\mu m^3$; scaffold only, $0.18 \pm 0.02\ \mu m/\mu m^3$; fig. S6). We further validated these measurements by analyzing the same region (medial proximal femoral cortex) in nonoperated (control) femurs ($0.20 \pm 0.04\ \mu m/\mu m^3$; fig. S6), which showed similar canalicular density to the native cortex in each group (Fig. 4, D to F). In general for all groups, native mouse cortex regions displayed very organized ECM with collagen fibers almost parallel to each other (fig. S6). In this way, native cortex regions were much more organized compared to those within the ossicle of hCol$^+$ trabeculae (Fig. 3F) and even with those from mCherry$^+$ trabeculae (Fig. 3C). Thus, differences in terms of canalicular density between native mouse bone and newly formed (mCherry$^+$, hCol$^+$) bone were also reflected in their collagen organization.

We found not only composite patterns of human (hCol$^+$) and mouse (hCol$^-$) trabeculae (Fig. 2, C and E, and fig. S4, F and G) but also patchy hCol$^+$ and hCol$^-$ staining within individual trabecula (Fig. 4, A and B). Again, hCol$^+$ regions within the hybrid trabecula exhibited larger lacunae and sparser canalicular density, with respect to the hCol$^-$ region [see dashed versus solid line in Fig. 4 (A and B)]. Importantly, no clear boundaries were found between hCol$^+$ and hCol$^-$ regions, but rather, the two networks appeared to be interconnected within the same tissue, as shown by the stacked image renderings of the same area (Fig. 4, B and C, and movie S2). Together, these data support the hypothesis that species-specific architectural differences are maintained despite the structural integration of human and mouse tissue in a humanized bone organ.

Human bone continues to be laid down and remodeled after 6 weeks in vivo

We previously showed that hOBs were present around trabecular bone and colocalized with human stromal tissue (Fig. 2, E and F),

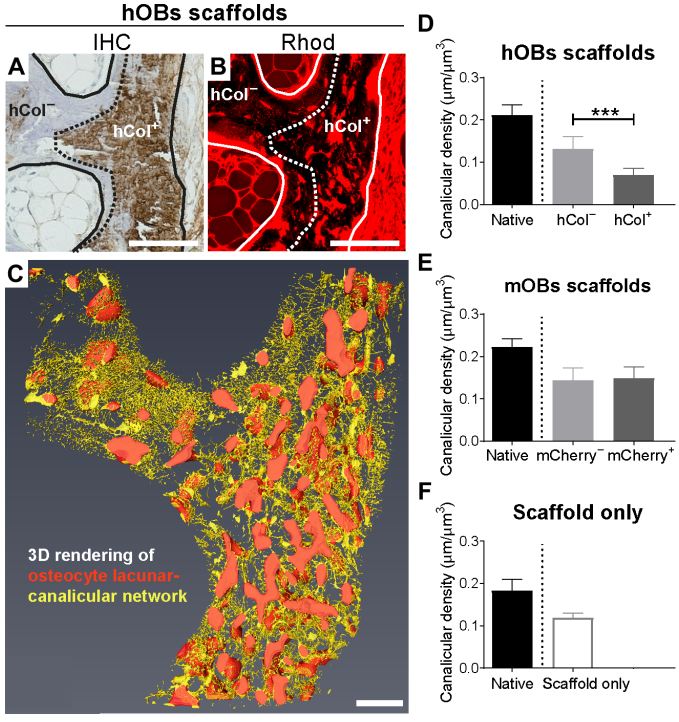

Fig. 4. Human and mouse collagen integrate in bone tissue while maintaining their species-specific differences at the osteocyte LCN level. (**A** to **C**) Correlative imaging of hOBs-seeded scaffolds following (A) hCol IHC and (B) rhodamine (Rhod) staining of the LCN imaged with confocal microscopy. (C) 3D rendering of the z-stack obtained from (B). The dashed line separates hCol$^-$- from hCol$^+$-stained areas within the same trabecula (solid line). (**D** to **F**) Canalicular density was evaluated in scaffolds with human (hOBs), mouse (mOBs), or no osteoblasts (scaffold only) and in three ROIs: trabeculae IHC negative, trabeculae IHC positive, and medial proximal native cortex as internal bone mouse control. (D to F) Data represent means ± SD, paired t test, ***$P < 0.0001$, $n = 8$ to 10 ROIs per animal, and $N = 6$ animals per group. Scale bars, 100 μm.

indicative of an ongoing process of matrix deposition. However, while both mOBs and hOBs scaffolds were implanted in vivo under the same conditions, mCherry$^+$ trabeculae showed a lamellar-like tissue organization compared to the woven-like collagen arrangement of hCol$^+$ trabeculae, suggesting differences in tissue remodeling. To understand why human collagen still displayed a woven morphology 6 weeks after implantation, we investigated the ability of the ossicle microenvironment to form and remodel human bone. The three-dimensional (3D) registration of in vivo microCT scans for weeks 4 to 6 allowed us to distinguish areas of newly formed bone (blue), resorbed bone (red), and quiescent bone (yellow). Since the scans were done in relatively long (2 week) interval, the contralateral (nonoperated) control femur of the same animal was also registered as control. 3D registration showed mostly quiescent areas in the control femur, although resorption and formation regions were present as well (Fig. 5A). The remodeling observed in the control femur was expected because of the age of the animals (weeks 9 and 11) at the time of the CT scans. hOBs scaffold–implanted femur 3D registration showed evidence of both formation and resorption within the ossicle, which provides evidence of bone remodeling (and not resorption only) within the humanized ossicle (Fig. 5A).

In agreement with these findings, we found a newly formed human tissue in regions of poorly mineralized, immature human

collagen surrounded by a dense collagenous matrix and scaffold fibers [see dashed lines in Fig. 5 (E to I)]. This immature collagen type I tissue was mostly transparent to backscattered electron correlative microscopy, which evidenced the low mineral content in comparison with the neighboring trabeculae (see dashed and solid lines in Fig. 5E). Moreover, correlative imaging with confocal microscopy showed the same tissue abundantly stained with rhodamine, in contrast to the weak staining of mineralized tissue where the dye was not able to penetrate (see dashed and solid lines in Fig. 5F). In contrast to previously shown hCol$^+$ trabeculae, no canaliculi or lacunae were evident [compare Fig. 3 (B and E) with Fig. 5F], indicative of no osteocyte formation. Moreover, the disorganized aspect of the matrix visible in histological analysis was confirmed by a poorly organized, woven-like bone collagen mesh, captured with SHG imaging (Fig. 5, G and I). Positive hCol and hOCalcin staining was present even 31 weeks after ectopic implantation of hOBs-seeded scaffolds (fig. S8), demonstrating the long-term presence of human compartment. To exclude the possibility that human bone regions experience more or less resorption due to the species difference with the host microenvironment, we examined the presence of osteoclast in both hCol$^-$ and hCol$^+$ within the ossicle. Quantification of number of osteoclasts per bone surface showed no significant differences between mouse and human collagen in hOBs scaffolds, suggesting that human osteocyte/osteoblast communication with mouse osteoclasts was not impaired (Fig. 5, B to D). Together, these results indicate that living human bone tissue in a mouse environment

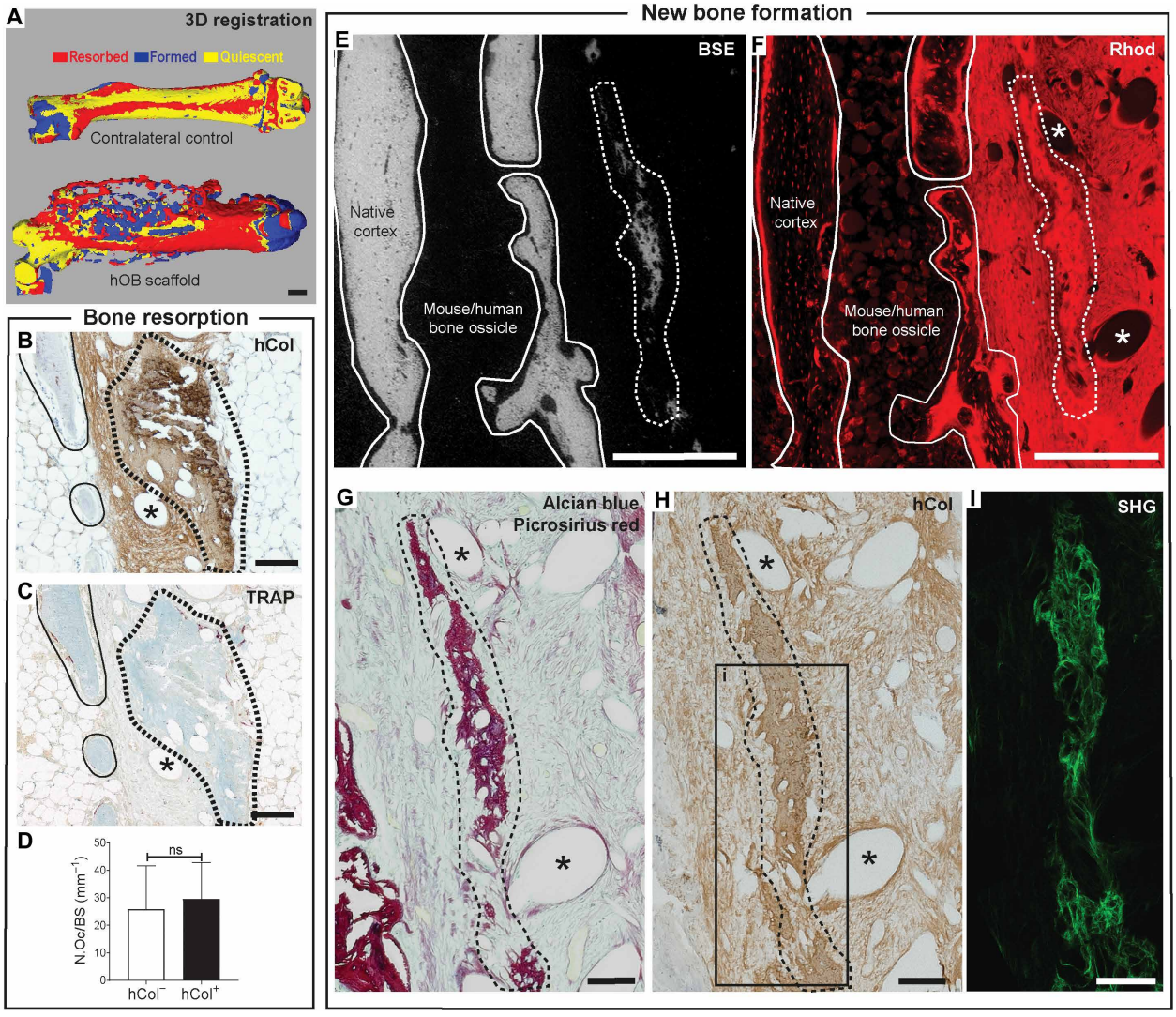

Fig. 5. New human collagen continues to be laid down 6 weeks after implantation of hOBs-seeded scaffolds. (**A**) 3D registration of 4- to 6-week in vivo microCT scans displaying resorbed (red), newly formed (blue), and quiescent (yellow) bone. (**B** to **D**) Bone resorption of hCol$^+$ (dashed lines) regions compared to hCol$^-$ regions (solid lines) within the human/mouse bone. (B and C) Consecutive sections stained with (B) hCol and (C) tartrate-resistant acid phosphatase (TRAP) to measure the (D) number of osteoclast (fuchsia) per bone surface (light blue) (N.Oc/BS, N.Oc/mm = mm^{-1}) in hCol$^-$ and hCol$^+$ areas. (**E** to **I**) Poorly mineralized, newly formed bone hCol$^+$ region (dashed lines) compared to mineralized hCol$^-$ bone regions (solid lines) within the human/mouse bone ossicle 6 weeks after implantation. Asterisk (*) indicates scaffold fibers. Correlative imaging of (E) mineral content with backscattered electron (BSE) microscopy, (F) LCN with rhodamine staining (Rhod) and confocal microscopy, (G) Alcian blue (proteoglycans) and Picrosirius red (collagen) staining, (H) hCol staining, and (I) collagen organization with SHG imaging. Data represent means ± SD; ns, not significant. $n = 4$ ROIs per animal, and $N = 3$ animals. Scale bars equal to 1000 μm (A), 100 μm (B, C, G, H, and I) and 500 μm (E and F).

is remodeled and can continue to be laid down and remodeled for up to at least 6 weeks in vivo.

DISCUSSION

In this study, we aimed to determine whether humanized bone resembles human or mouse bone ultrastructural properties. To do so, we tissue-engineered humanized bone at an orthotopic location. Consistent with previous studies, the humanized ossicle showed typical features of a bone organ, such as trabecular bone, bone marrow and vasculature, surrounded by a cortical-like bone shell (*5*, *9*, *14*). In agreement with previous studies, blood vessels within the ossicle were located at the vicinity of trabecular bone (*36*). Similar to previous publication, the addition of cells to the scaffold (either mouse or human) did not change bone volume (*14*), as it is known that BMP2 delivery is a key factor driving ectopic bone formation (*9*, *18*–*20*, *37*). Previous studies have shown that the amount of bone formed ectopically depends on the initial dose of BMP (*18*). Previous doses of BMP7 delivered with a fibrin hydrogel ranged from 10 to 30 μg (*10*, *14*, *19*) and 20 to 30 μg in the case of BMP2 (*6*, *12*). These are rather large doses of BMP when considering the desired controlled release of lower doses for bone regeneration (*38*, *39*) yet commonly required in the field of ectopic bone formation (*6*, *10*, *12*, *14*, *19*). Since, in the present study, we delivered a 20-μg BMP2 dose at an orthotopic location (i.e., mouse femur), future studies should explore the dose impact on the remodeling at the host bone/ossicle junction. As humanized bone ossicles are often used in the context of bone metastasis (*10*, *40*, *41*), smaller BMP doses would result in smaller bone ossicles, which might be resorbed by osteolytic lesions before the end of the study end point.

Here, we show a complete overview and detailed images of hCol and hOCalcin IHC staining, which demonstrate the blend of human and mouse ECM composition of humanized bone and an orthotopic site. Moreover, we performed IHC analysis in mineralized resin sections, which allowed the evaluation of ECM organization and the correlation and colocalization with the LCN.

The LCN analyses from mouse trabeculae (scaffold only, $mCherry^+$, $mCherry^-$, and $hCol^-$), formed under the same conditions as $hCol^+$ regions, were consistent with previous analysis in disorganized regions from mouse native bone (*31*). In contrast to this, the aforementioned [scaffold only, $mCherry^+$, $mCherry^-$, and $hCol^-$ and previous study (*31*)] canalicular densities differed from the regions of highly organized, native cortical mouse bone (0.20 ± 0.01 μm/μm^3). It is known that the cross-section of murine cortical bone displays a well-organized circumferential lamellae near the endosteum and periosteum and a more disorganized, woven-like matrix toward the center (*22*, *30*). This explains the differences in canalicular densities between disorganized (0.10 ± 0.01 μm/μm^3) (*31*) and organized (0.20 ± 0.01 μm/μm^3) regions in native mouse bone.

The LCN analysis showed that human collagen regions, identified by IHC, had lower canalicular density and larger lacuna volume with respect to those of mouse collagen in mOBs scaffolds, scaffold only, and even compared to those of the $hCol^-$ regions. Previous studies in human osteonal bone showed comparable canalicular density (0.074 ± 0.015 μm/μm^3) (*28*, *42*) and therefore supports the hypothesis that $hCol^+$ regions formed within the ossicle have a human-like bone ultrastructure. Moreover, the canalicular network in disorganized collagen $hCol^+$ regions was lower than the one reported in previous studies looking at disorganized collagen regions in mouse bone (0.10 ± 0.01 μm/μm^3) (*31*), which again supports our species-specific ultrastructural differences hypothesis.

One limitation of the present study is that, because of the large lacuna volume in $hCol^+$ regions with respect to the total analyzed volume, the average lacuna volume in $hCol^+$ regions was underestimated. Because of the complex, disorganized matrix of $hCol^+$ regions, it was not feasible to enlarge the total analyzed volume by acquiring larger *z*-stacks, which remains a technical limitation in our analysis. Despite this, we observed that $hCol^+$ regions had a higher lacuna volume compared to those from mouse origin, which was a consistent finding with respect to the lower canalicular density and the disorganized matrix. In the literature, these values oscillated between 293 and 502 μm^3 in human bone (*43*, *44*), while for mouse bone, the range was broader (154 to 575 μm^3) (*45*–*47*). The previous values are difficult to directly compare with the results presented here, as the measurements were acquired with different imaging techniques and resolutions and the specimens differed in age, strain, and anatomical region (*43*–*47*). Another limitation is that reference values for LCN density measurements are restricted to healthy adult human femoral osteonal and murine femoral bone regions, as, up to now, there is a lack of quantitative data from other anatomical sites or conditions in the literature.

Last, we probed whether the differences in collagen organization between human and mouse regions were due to different species-specific remodeling rates. Our results showed that $hCol^+$ trabeculae were resorbed at the same rate as $hCol^-$ (mouse) trabeculae and that hOBs cells were still active, as evidenced by the new human bone matrix deposition 6 weeks after scaffold implantation. Further studies, beyond the scope of the present manuscript, would be required to assess the evolution of human-specific bone structures over time and, therefore, the best window of usability of this model.

In conclusion, we have identified that mouse and human-like tissue types coexist and structurally integrate in a chimeric bone organ while maintaining species-specific ultrastructural differences by using a comprehensive multiscale analysis. These results emphasize the need for validating immunohistochemical analysis against a multiscale materials science–based methodology, which can be of great scientific value to further develop and enhance human-like physiology in humanized mouse models.

MATERIALS AND METHODS

Cell culture

hOBs were isolated from a 64-year-old female undergoing hip replacement (Queensland University of Technology Human Research Ethics Committee approval number 1400001024) and cultured in basal media [α minimum essential medium (Life Technologies), 10% fetal calf serum (Lonza, catalog no. 14-506F), and penicillin (100 IU/ml) and streptomycin (100 μg/ml) (Life Technologies, catalog no. 15140-122)]. Alizarin red staining was conducted to evaluate the mineralization ability of patient-derived cells before scaffold cell seeding (fig. S2A). Cells were incubated at 37°C and 5% CO_2, and medium was replaced every 3 to 4 days. Mouse primary osteoblasts (mOBs) were isolated from the femur of a 12-week-old NSG mouse. Following expansion, mOBs were transduced with mCherry lentivirus and positive cells were isolated using fluorescence-activated cell sorting (FACS; FACSAria III, BD Biosciences, USA). The mCherry signal after FACS and cell expansion was confirmed by fluorescence microscopy. Culture conditions were identical as for hOBs.

Medical-grade polycaprolactone (mPCL; 50 kDa) scaffolds were melt electrospun written (inner diameter, 2.7 mm; outer diameter, 3 mm) and calcium phosphate–coated to improve the adhesion as described in (*9*) (fig. S1A). Primary hOBs (80,000 cells per scaffold) from the same donor were seeded on the mPCL scaffolds as described in (*9*) and cultured in vitro for 2 weeks in basal media and three additional weeks in osteogenic media [basal media supplemented with L-ascorbic acid-2-phosphate (50 μg/ml; Sigma-Aldrich, A8960), 10 mM β-glycerophosphate (Sigma-Aldrich, G9891), and 0.1 μM dexamethasone (Sigma-Aldrich, D2915)]. Scaffold/cell constructs were incubated at 37°C and 5% CO_2, and medium was replaced every 3 to 4 days. Constructs were characterized in vitro with viability and differentiation assays before in vivo implantation (fig. S2, B to D).

Animal experiments

All animal experiments were approved by the University of Queensland Animal Ethics Committee (approval number QUT/IHBI/376/14/ARC) in accordance with the Australian Code of Practice for the Care and Use of Animals for Scientific Purposes. Female NOD-scid IL2Rγnull (NOD.Cg–*Prkdc*^{scid} *Il2rg*^{tm1Wjl}/SzJ; NSG) mice were obtained from the Animal Resource Centre (Canning Vale, WA, Australia) at 4 weeks of age. Animals were housed at the Translational Research Institute, maintained under specific pathogen–free and temperature-controlled conditions, and allowed to acclimatize for 1 week before experimentation. Sterilized food and water were provided ad libitum, and mice were kept on a 12-hour light/12-hour dark cycle.

hOBs-seeded scaffolds ($N = 6$), mOB-seeded scaffolds ($N = 6$), or scaffold only ($N = 6$) were orthotopically implanted around the lateral part of the right femur diaphysis of 5-week-old female NSG mice as described in (*9*). Briefly, a mixture of 20 μl of fibrin glue (TISSEEL Fibrin Sealant, Baxter Healthcare International, USA) with 13.3 μl of human recombinant BMP2 (20 μg of BMP2; InductOs, Medtronic BioPharma) was placed between the scaffold and implanted around the lateral part of the bone femur diaphysis (Fig. 1A). Animals recovered within 12 to 14 hours from the surgery with no signs of limb paralysis. Animals were scanned with in vivo CT (36-μm pixel size, 80 kV, 500 μA) every 2 weeks (Inveon, Siemens Medical Solutions, Knoxville, TN). After 6 to 7 weeks in vivo, animals were euthanized, and orthotopically implanted (right) and nonoperated control (left) femurs were dissected and fixed in 4% paraformaldehyde in phosphate-buffered saline.

The 3D registration was performed by aligning in vivo scans from weeks 4 and 6using DataViewer (Bruker, Kontich, Belgium) as described in (*48*). Aligned datasets were then registered to identify formation and resorption sites using 3D dynamic in vivo morphometry as described in (*49*).

Specimen processing and resin embedding

Specimens were processed for cold polymethyl methacrylate (PMMA) embedding following the manufacturer's instructions (Technovit 9100, Kulzer, Germany). In short, specimens were dehydrated in increasing concentrations of ethanol, stained with rhodamine solution [0.417 g of Rhodamine 6G (ACROS Organics, Belgium) per 100 ml of ethanol], cleared with xylol, and then infiltrated and polymerized with PMMA.

Ex vivo microCT

Specimens were scanned using an EasyTom micro/nano tomograph (RX Solutions, France). Scanning parameters were as follows: 107 kV, 93 μA, 7-μm voxel size, frame rate of 3, and average frame of 5. Reconstruction of the 1120 projections per scan were performed using RX Solutions X-Act software; image analysis was performed using ImageJ (*50*) and CTAn (Bruker, Kontich, Belgium), and visualization was performed using Amira software.

Histology

Consecutive and numbered PMMA sections (5 to 6 μm in thickness) were stained for Alcian blue and Picrosirius red staining, IHC, and tartrate-resistant acid phosphatase (TRAP). Alcian blue and Picrosirius red staining was done with 0.5% Alcian blue 8GX (A5268-10G, Sigma-Aldrich) for proteoglycan-rich cartilage matrix (blue) and 1% Picrosirius red F3B (365548-5G, Sigma-Aldrich) for collagen (red). TRAP staining and analysis were performed as described in (*51*); results were expressed as the number of osteoclast per bone surface (N/mm = mm^{-1}). IHC for hCol (ab138492), hNuma (ab97585), hOCalcin (ab13420), and mCherry (NBP2-25157) was performed as described (table S1). Images were captured with a KEYENCE digital microscope (VHX-5550E, Keyence, Germany).

Confocal laser scanning microscopy and SHG fluorescence imaging

Following sectioning, the exposed PMMA block surface of the specimens was imaged with confocal laser scanning microscopy (Leica TCS SP8 DLS, Multiphoton, Germany) using $\lambda_{excitation}$ = 514-nm argon laser light/$\lambda_{emission}$ = 550- to 650-nm laser light. For LCN analyses, images were acquired with a resolution of 1024 pixels by 1024 pixels (field of view, 388 μm by 388 μm; pixel size, 378 nm^2), and around 120 images with a thickness of 0.3 μm were made over 30 to 40 μm in depth of the block. The depth of imaging was restricted to about 30 to 40 μm because of the attenuation of the fluorescent radiation through the mineralized sample. To compensate for the loss of signal when scanning along the depth, laser intensity and photomultiplier gain were continuously increased. SHG imaging was performed on the exact same ROI with a pulsed infrared laser ($\lambda_{excitation}$ = 910 nm/$\lambda_{emission}$ = 450 to 460 nm). One SHG image from the block surface was collected per ROI. This SHG image was then qualitatively classified as lamellar-like (collagen fibers not crossing each other; Fig. 3C), intermediate, or woven-like (collagen mesh; Fig. 4F). For each treatment (hOBs, mOBs, and scaffold only), the total number of images corresponding to each category was normalized to the bone volume in each ROI measured with confocal microscopy and displayed as percentage. A minimum of 2 to 3 unit volumes were analyzed per type of ROI (n = 2 to 3) and animal, with six animals per treatment ($N = 6$).

LCN analysis and code availability statement

Only trabeculae within the human/mouse ossicle (i.e., excluding the ossicle shell and lateral femoral cortex) were included for analysis, as these regions appeared purely murine. IHC against hCol or mCherry was used to detect ROIs that were either fully stained (hCol$^+$ and mCherry$^+$ groups) or not stained (hCol$^-$ and mCherry$^-$ groups) in hOBs scaffold and mCherry mOB scaffold treatments, respectively. Measurements on the medial proximal cortex were included in operated and nonoperated (contralateral) femurs as internal controls for native (11-week-old) mouse tissue. A minimum of 2 to 3 unit volumes were analyzed per type of ROI (n = 2 to 3) and animal, with six animals per treatment ($N = 6$).

For the network characterization, we used an established protocol based on (*28*, *31*, *52*). Here, we provide a short summary of the method [more detailed information can be found in (*28*, *31*, *52*) and in the Python (version 3.5) open source of the Tool for Image and Network Analysis (www.bitbucket.org/refelix/TINA)]. In short, raw confocal laser scanning microscopy data were segmented on the basis of the difference of Gaussians, which allowed us to automatically distinguish between canaliculi and lacunae on the basis of their bulkiness. Parameters for lacuna segmentation were chosen to gain reliable and robust results, i.e., insensitive for noise and differences in the staining intensity. All datasets were then evaluated with the same segmentation parameter set. The average lacuna volume was calculated by counting segmented lacuna voxels and dividing by the total number of lacunae. Our analysis includes incomplete lacunae, as lacuna size was relatively large with respect to the thickness of the ROI (maximal depth of 30 to 40 μm). Because of this, the average lacuna volume is underestimated in this analysis, particularly in datasets with larger lacunae. The segmented canaliculi were then skeletonized and rendered into a 3D network for further quantitative analysis. Using this network, we then computed the canalicular density, which quantifies the total length of canaliculi per unit bone volume, excluding lacuna volume.

Backscattered electron microscopy

The exposed PMMA block surface of the specimens was imaged with an environmental scanning electron microscope (FEI FEG-ESEM Quanta 600, FEI Company, USA) in backscattered electron mode, without polishing to ensure that the correlative multimodal imaging was performed in the exact same region. The following settings were used: 10 to 12.5 kV, low vacuum conditions (0.75 torr), working distance of approximately 10 mm, and various magnifications (×400 to ×1000).

Statistical analysis

All experimental data were analyzed using Statistical Analysis SPSS Base 16.0 software for Windows. Results were expressed as means ± SD and plotted using GraphPad Prism. Normal distribution of the data was confirmed by the Kolmogorov-Smirnov test. Comparisons between treatments were performed using one-way ANOVA test and Tukey's post hoc test. Comparisons between two groups of the same treatment were performed with a paired *t* test. Only two-tailed statistical tests were used, and values of $P < 0.05$ were considered statistically significant.

SUPPLEMENTARY MATERIALS

Supplementary material for this article is available at http://advances.sciencemag.org/cgi/content/full/6/44/eabb9265/DC1

REFERENCES AND NOTES

1. M. de Jong, T. Maina, Of mice and humans: Are they the same?—Implications in cancer translational research. *J. Nucl. Med.* **51**, 501–504 (2010).
2. L. D. Shultz, F. Ishikawa, D. L. Greiner, Humanized mice in translational biomedical research. *Nat. Rev. Immunol.* **7**, 118–130 (2007).
3. R. Ito, T. Takahashi, I. Katano, M. Ito, Current advances in humanized mouse models. *Cell. Mol. Immunol.* **9**, 208–214 (2012).
4. F. Zhu, R. R. Nair, E. M. C. Fisher, T. J. Cunningham, Humanising the mouse genome piece by piece. *Nat. Commun.* **10**, 1845 (2019).
5. B. M. Holzapfel, D. W. Hutmacher, B. Nowlan, V. Barbier, L. Thibaudeau, C. Theodoropoulos, J. D. Hooper, D. Loessner, J. A. Clements, P. J. Russell, A. R. Pettit, I. G. Winkler, J.-P. Levesque, Tissue engineered humanized bone supports human hematopoiesis in vivo. *Biomaterials* **61**, 103–114 (2015).
6. J. E. Moreau, K. Anderson, J. R. Mauney, T. Nguyen, D. L. Kaplan, M. Rosenblatt, Tissue-engineered bone serves as a target for metastasis of human breast cancer in a mouse model. *Cancer Res.* **67**, 10304–10308 (2007).
7. Y. Chen, R. Jacamo, Y.-x. Shi, R.-y. Wang, V. L. Battula, S. Konoplev, D. Strunk, N. A. Hofmann, A. Reinisch, M. Konopleva, M. Andreeff, Human extramedullary bone marrow in mice: A novel in vivo model of genetically controlled hematopoietic microenvironment. *Blood* **119**, 4971–4980 (2012).
8. I. Kurelac, A. Abarrategi, M. Ragazzi, L. Iommarini, N. U. Ganesh, T. Snoeks, D. Bonnet, A. M. Porcelli, I. Malanchi, G. Gasparre, A humanized bone niche model reveals bone tissue preservation upon targeting mitochondrial complex I in pseudo-orthotopic osteosarcoma. *J. Clin. Med.* **8**, 2184 (2019).
9. L. C. Martine, B. M. Holzapfel, J. A. McGovern, F. Wagner, V. M. Quent, P. Hesami, F. M. Wunner, C. Vaquette, E. M. De-Juan-Pardo, T. D. Brown, B. Nowlan, D. J. Wu, C. O. Hutmacher, D. Moi, T. Oussenko, E. Piccinini, P. W. Zandstra, R. Mazzieri, J. Lévesque, P. D. Dalton, A. V. Taubenberger, D. W. Hutmacher, Engineering a humanized bone organ model in mice to study bone metastases. *Nat. Protoc.* **12**, 639–663 (2017).
10. V. Quent, A. Taubenberger, J. Reichert, L. Martine, J. Clements, D. Hutmacher, D. Loessner, A humanised tissue-engineered bone model allows species-specific breast cancer-related bone metastasis in vivo. *J. Tissue Eng. Regen. Med.* **12**, 494–504 (2018).
11. M. L. Muerza-Cascante, D. Haylock, D. W. Hutmacher, P. D. Dalton, Melt electrospinning and its technologization in tissue engineering. *Tissue Eng. Part B Rev.* **21**, 187–202 (2015).
12. M. Landgraf, C. A. Lahr, A. Sanchez-Herrero, C. Meinert, A. Shokoohmand, P. M. Pollock, D. W. Hutmacher, A. Shafiee, J. A. McGovern, Humanized bone facilitates prostate cancer metastasis and recapitulates therapeutic effects of zoledronic acid in vivo. *Bone Res.* **7**, 31 (2019).
13. F. Wagner, B. M. Holzapfel, L. C. Martine, J. McGovern, C. A. Lahr, M. Boxberg, P. M. Prodinger, S. Grässel, D. Loessner, D. W. Hutmacher, A humanized bone microenvironment uncovers HIF2 alpha as a latent marker for osteosarcoma. *Acta Biomater.* **89**, 372–381 (2019).
14. F. Wagner, B. M. Holzapfel, J. A. McGovern, A. Shafiee, J. G. Baldwin, L. C. Martine, C. A. Lahr, F. M. Wunner, T. Friis, O. Bas, M. Boxberg, P. M. Prodinger, A. Shokoohmand, D. Moi, R. Mazzieri, D. Loessner, D. W. Hutmacher, Humanization of bone and bone marrow in an orthotopic site reveals new potential therapeutic targets in osteosarcoma. *Biomaterials* **171**, 230–246 (2018).
15. J. Lee, M. Li, J. Milwid, J. Dunham, C. Vinegoni, R. Gorbatov, Y. Iwamoto, F. Wang, K. Shen, K. Hatfield, M. Enger, S. Shafiee, E. McCormack, B. L. Ebert, R. Weissleder, M. L. Yarmush, B. Parekkadan, Implantable microenvironments to attract hematopoietic stem/cancer cells. *Proc. Natl. Acad. Sci. U.S.A.* **109**, 19638–19643 (2012).
16. A. Reinisch, D. Thomas, M. R. Corces, X. Zhang, D. Gratzinger, W.-J. Hong, K. Schallmoser, D. Strunk, R. Majeti, A humanized bone marrow ossicle xenotransplantation model enables improved engraftment of healthy and leukemic human hematopoietic cells. *Nat. Med.* **22**, 812–821 (2016).
17. J. McGovern, A. Shafiee, F. Wagner, C. Lahr, M. Landgraf, C. Meinert, E. Williams, P. Russell, J. Clements, D. Loessner, B. Holzapfel, G. Risbridger, D. Hutmacher, Humanization of the prostate microenvironment reduces homing of PC3 prostate cancer cells to human tissue-engineered bone. *Cancers* **10**, 438 (2018).
18. F. P. Seib, J. E. Berry, Y. Shiozawa, R. S. Taichman, D. L. Kaplan, Tissue engineering a surrogate niche for metastatic cancer cells. *Biomaterials* **51**, 313–319 (2015).
19. F. Wagner, B. M. Holzapfel, L. Thibaudeau, M. Straub, M.-T. Ling, J. Grifka, D. Loessner, J.-P. Lévesque, D. W. Hutmacher, A validated preclinical animal model for primary bone tumor research. *J. Bone Joint Surg.* **98**, 916–925 (2016).
20. C. A. Lahr, F. Wagner, A. Shafiee, M. Rudert, D. W. Hutmacher, B. M. Holzapfel, Recombinant human bone morphogenetic protein 7 exerts osteo-catabolic effects on bone grafts that outweigh its osteo-anabolic capacity. *Calcif. Tissue Int.* **105**, 331–340 (2019).
21. C. Stüdle, Q. Vallmajó-Martín, A. Haumer, J. Guerrero, M. Centola, A. Mehrkens, D. J. Schaefer, M. Ehrbar, A. Barbero, I. Martin, Spatially confined induction of endochondral ossification by functionalized hydrogels for ectopic engineering of osteochondral tissues. *Biomaterials* **171**, 219–229 (2018).
22. M. Kerschnitzki, W. Wagermaier, P. Roschger, J. Seto, R. Shahar, G. N. Duda, S. Mundlos, P. Fratzl, The organization of the osteocyte network mirrors the extracellular matrix orientation in bone. *J. Struct. Biol.* **173**, 303–311 (2011).
23. M. M. Giraud-Guille, Twisted plywood architecture of collagen fibrils in human compact bone osteons. *Calcif. Tissue Int.* **42**, 167–180 (1988).
24. L. F. Bonewald, The amazing osteocyte. *J. Bone Miner. Res.* **26**, 229–238 (2011).
25. F. He, A. E. Chiou, H. C. Loh, M. Lynch, B. R. Seo, Y. H. Song, M. J. Lee, R. Hoerth, E. L. Bortel, B. M. Willie, G. N. Duda, L. A. Estroff, A. Masic, W. Wagermaier, P. Fratzl, C. Fischbach, Multiscale characterization of the mineral phase at skeletal sites of breast cancer metastasis. *Proc. Natl. Acad. Sci.* **114**, 10542–10547 (2017).
26. M. B. Schaffler, W.-Y. Cheung, R. Majeska, O. Kennedy, Osteocytes: Master orchestrators of bone. *Calcif. Tissue Int.* **94**, 5–24 (2014).

27. F. Repp, P. Kollmannsberger, A. Roschger, A. Berzlanovich, G. M. Gruber, P. Roschger, W. Wagermaier, R. Weinkamer, Coalignment of osteocyte canaliculi and collagen fibers in human osteonal bone. *J. Struct. Biol.* **199**, 177–186 (2017).
28. F. Repp, P. Kollmannsberger, A. Roschger, M. Kerschnitzki, A. Berzlanovich, G. M. Gruber, P. Roschger, W. Wagermaier, R. Weinkamer, Spatial heterogeneity in the canalicular density of the osteocyte network in human osteons. *Bone Rep.* **6**, 101–108 (2017).
29. M. Kerschnitzki, W. Wagermaier, Y. Liu, P. Roschger, G. N. Duda, P. Fratzl, Poorly ordered bone as an endogenous scaffold for the deposition of highly oriented lamellar tissue in rapidly growing ovine bone. *Cells Tissues Organs* **194**, 119–123 (2011).
30. A. Shipov, P. Zaslansky, H. Riesemeier, G. Segev, A. Atkins, R. Shahar, Unremodeled endochondral bone is a major architectural component of the cortical bone of the rat (*Rattus norvegicus*). *J. Struct. Biol.* **183**, 132–140 (2013).
31. P. Kollmannsberger, M. Kerschnitzki, F. Repp, W. Wagermaier, R. Weinkamer, P. Fratzl, The small world of osteocytes: Connectomics of the lacuno-canalicular network in bone. *New J. Phys.* **19**, 073019 (2017).
32. C. S. Yee, C. A. Schurman, C. R. White, T. Alliston, Investigating osteocytic perilacunar/canalicular remodeling. *Curr. Osteoporos. Rep.* **17**, 157–168 (2019).
33. P. Hesami, B. M. Holzapfel, A. Taubenberger, M. Roudier, L. Fazli, S. Sieh, L. Thibaudeau, L. S. Gregory, D. W. Hutmacher, J. A. Clements, A humanized tissue-engineered in vivo model to dissect interactions between human prostate cancer cells and human bone. *Clin. Exp. Metastasis* **31**, 435–446 (2014).
34. A. Shafiee, J. A. McGovern, C. A. Lahr, C. Meinert, D. Moi, F. Wagner, M. Landgraf, E. De-Juan-Pardo, R. Mazzieri, D. W. Hutmacher, Immune system augmentation via humanization using stem/progenitor cells and bioengineering in a breast cancer model study. *Int. J. Cancer* **143**, 1470–1482 (2018).
35. R. Das, T. Strowig, R. Verma, S. Koduru, A. Hafemann, S. Hopf, M. H. Kocoglu, C. Borsotti, L. Zhang, A. Branagan, E. Eynon, M. G. Manz, R. A. Flavell, M. V. Dhodapkar, Microenvironment-dependent growth of preneoplastic and malignant plasma cells in humanized mice. *Nat. Med.* **22**, 1351–1357 (2016).
36. S. J. Morrison, D. T. Scadden, The bone marrow niche for haematopoietic stem cells. *Nature* **505**, 327–334 (2014).
37. S. S. Murray, E. J. B. Murray, J. C. Wang, M. E. L. Duarte, The history and histology of bone morphogenetic protein. *Histol. Histopathol.* **31**, 721–732 (2016).
38. A. Shekaran, J. R. García, A. Y. Clark, T. E. Kavanaugh, A. S. Lin, R. E. Guldberg, A. J. García, Bone regeneration using an alpha 2 beta 1 integrin-specific hydrogel as a BMP-2 delivery vehicle. *Biomaterials* **35**, 5453–5461 (2014).
39. B. Zhang, J. D. Skelly, J. R. Maalouf, D. C. Ayers, J. Song, Multifunctional scaffolds for facile implantation, spontaneous fixation, and accelerated long bone regeneration in rodents. *Sci. Transl. Med.* **11**, eaau7411 (2019).
40. F. Bersani, J. Lee, M. Yu, R. Morris, R. Desai, S. Ramaswamy, M. Toner, D. A. Haber, B. Parekkadan, Bioengineered implantable scaffolds as a tool to study stromal-derived factors in metastatic cancer models. *Cancer Res.* **74**, 7229–7238 (2014).
41. A. Reinisch, N. Etchart, D. Thomas, N. A. Hofmann, M. Fruehwirth, S. Sinha, C. K. Chan, K. Senarath-Yapa, E.-Y. Seo, T. Wearda, U. F. Hartwig, C. Beham-Schmid, S. Trajanoski, Q. Lin, W. Wagner, C. Dullin, F. Alves, M. Andreeff, I. L. Weissman, M. T. Longaker, K. Schallmoser, R. Majeti, D. Strunk, Epigenetic and in vivo comparison of diverse MSC sources reveals an endochondral signature for human hematopoietic niche formation. *Blood* **125**, 249–260 (2015).
42. A. F. van Tol, A. Roschger, F. Repp, J. Chen, P. Roschger, A. Berzlanovich, G. M. Gruber, P. Fratzl, R. Weinkamer, Network architecture strongly influences the fluid flow pattern through the lacunocanalicular network in human osteons. *Biomech. Model. Mechanobiol.* **19**, 823–840 (2019).
43. B. Hesse, N. Männicke, A. Pacureanu, P. Varga, M. Langer, P. Maurer, F. Peyrin, K. Raum, Accessing osteocyte lacunar geometrical properties in human jaw bone on the submicron length scale using synchrotron radiation μCT. *J. Microsc.* **255**, 158–168 (2014).
44. Y. Carter, C. D. L. Thomas, J. G. Clement, A. G. Peele, K. Hannah, D. M. L. Cooper, Variation in osteocyte lacunar morphology and density in the human femur—A synchrotron radiation micro-CT study. *Bone* **52**, 126–132 (2013).
45. P. Schneider, M. Stauber, R. Voide, M. Stampanoni, L. R. Donahue, R. Müller, Ultrastructural properties in cortical bone vary greatly in two inbred strains of mice as assessed by synchrotron light based micro- and nano-CT. *J. Bone Miner. Res.* **22**, 1557–1570 (2007).
46. A. Vatsa, R. G. Breuls, C. M. Semeins, P. L. Salmon, T. H. Smit, J. Klein-Nulend, Osteocyte morphology in fibula and calvaria—Is there a role for mechanosensing? *Bone* **43**, 452–458 (2008).
47. N. K. Wittig, M. Laugesen, M. E. Birkbak, F. L. Bach-Gansmo, A. Pacureanu, S. Bruns, M. H. Wendelboe, A. Brüel, H. O. Sørensen, J. S. Thomsen, H. Birkedal, Canalicular junctions in the osteocyte lacuno-canalicular network of cortical bone. *ACS Nano* **13**, 6421–6430 (2019).
48. I. Moreno-Jiménez, S. A. Lanham, J. M. Kanczler, G. Hulsart-Billstrom, N. D. Evans, R. O. C. Oreffo, Remodelling of human bone on the chorioallantoic membrane of the chicken egg: De novo bone formation and resorption. *J. Tissue Eng. Regen. Med.* **12**, 1877–1890 (2018).
49. A. I. Birkhold, H. Razi, G. N. Duda, R. Weinkamer, S. Checa, B. M. Willie, Mineralizing surface is the main target of mechanical stimulation independent of age: 3D dynamic in vivo morphometry. *Bone* **66**, 15–25 (2014).
50. C. A. Schneider, W. S. Rasband, K. W. Eliceiri, NIH Image to ImageJ: 25 years of image analysis. *Nat. Methods* **9**, 671–675 (2012).
51. R. J. van 't Hof, L. Rose, E. Bassonga, A. Daroszewska, Open source software for semi-automated histomorphometry of bone resorption and formation parameters. *Bone* **99**, 69–79 (2017).
52. A. Roschger, P. Roschger, W. Wagermaier, J. Chen, A. F. van Tol, F. Repp, S. Blouin, A. Berzlanovich, G. M. Gruber, K. Klaushofer, P. Fratzl, R. Weinkamer, The contribution of the pericanalicular matrix to mineral content in human osteonal bone. *Bone* **123**, 76–85 (2019).

Acknowledgments: We would like to express gratitude to J. Steffen, D. Werner, J. Baldwin, and E. Ren for technical support; to S. Young for help with the 3D registration; and to G. Korus and A. Petersen for help with histology. **Funding:** D.W.H. acknowledges funding from the NHMRC Project Grant 1082313, the National Breast Cancer Foundation (NBCF IN-15-047), a grant from the Worldwide Cancer Research (WWCR 15-11563), and Humboldt Research Award. I.M.-J. acknowledges the postdoctoral fellowship from the Humboldt Foundation. A.C. acknowledges funding from the German Research Foundation (DFG) Emmy Noether grant CI 203/2-1. **Author contributions:** Study design: I.M.-J., A.C., D.W.H., and P.F. Experimental work: I.M.-J., A.S.-H., C.A.L., A.R., and J.A.M. Data analysis: I.M.-J. and A.F.v.T. Data interpretation: I.M.-J., A.C., D.W.H., and P.F. Drafting the manuscript: I.M.-J. Revising manuscript content and approving final version: All authors. **Competing interests:** The authors declare that they have no competing interests. **Data and materials availability:** All data needed to evaluate the conclusions in the paper are present in the paper and/or the Supplementary Materials. Additional data related to this paper may be requested from the authors.

Submitted 31 March 2020
Accepted 31 August 2020
Published 28 October 2020
10.1126/sciadv.abb9265

Citation: I. Moreno-Jiménez, A. Cipitria, A. Sánchez-Herrero, A. F. van Tol, A. Roschger, C. A. Lahr, J. A. McGovern, D. W. Hutmacher, P. Fratzl, Human and mouse bones physiologically integrate in a humanized mouse model while maintaining species-specific ultrastructure. *Sci. Adv.* **6**, eabb9265 (2020).

Science Advances

Human and mouse bones physiologically integrate in a humanized mouse model while maintaining species-specific ultrastructure

I. Moreno-Jiménez, A. Cipitria, A. Sánchez-Herrero, A. F. van Tol, A. Roschger, C. A. Lahr, J. A. McGovern, D. W. Hutmacher and P. Fratzl

Sci Adv **6** (44), eabb9265.
DOI: 10.1126/sciadv.abb9265